Distribution Agreement

In presenting this thesis as a partial fulfillment of the requirements for a degree from Emory University, I hereby grant to Emory University and its agents the non-exclusive license to archive, make accessible, and display my thesis in whole or in part in all forms of media, now or hereafter now, including display on the World Wide Web. I understand that I may select some access restrictions as part of the online submission of this thesis. I retain all ownership rights to the copyright of the thesis. I also retain the right to use in future works (such as articles or books) all or part of this thesis.

Siqi Xue April 3, 2017

Influences of Axial Symmetry of Arterial Stenosis on Pressure Distribution Based on Computational Fluid Dynamics Simulations

By

Siqi Xue

Alessandro Veneziani
Advisor

Alex Viguerie
Co-Advisor

Department of Mathematics and Computer Science

Alessandro Veneziani
Advisor

Lars Ruthotto
Committee Member

Michael Page
Committee Member

2017

Influences of Axial Symmetry of Arterial Stenosis on Pressure Distribution Based on Computational Fluid Dynamics Simulations

By

Siqi Xue

Alessandro Veneziani
Advisor

Alex Viguerie
Co-Advisor

An abstract of
a thesis submitted to the Faculty of Emory College of Arts and Sciences
of Emory University in partial fulfillment
of the requirements of the degree of
Bachelor of Sciences with Honors

Department of Mathematics and Computer Science

2017

Abstract

Influences of Axial Symmetry of Arterial Stenosis on Pressure Distribution Based on Computational Fluid Dynamics Simulations

By Siqi Xue

In this thesis, we want to find the degree of impact stenosis geometric features, especially the axial symmetry, can have on the pressure drop along the side walls of stenotic arterial vessels. Computational fluid dynamics (CFD) simulations are applied to solve the three-dimensional steady Navier-Stokes equations, a time-independent system characterizing incompressible, Newtonian, homogeneous flow and commonly used in blood flow models. The numerical solutions are computed using Finite Element approximation, and linearization of the system is done by Picard iteration method. As a result, we found that pressure drop can serve as an indicator for the geometric shape, especially the axial symmetricity, in cases of significant arterial stenosis. While for mild stenosis, pressure drop is not sufficiently informative in distinguishing between axisymmetric and nonsymmetric stenosis geometries.

Influences of Axial Symmetry of Arterial Stenosis on Pressure Distribution Based on Computational Fluid Dynamics Simulations

By

Siqi Xue

Alessandro Veneziani
Advisor

Alex Viguerie
Co-Advisor

A thesis submitted to the Faculty of Emory College of Arts and Sciences
of Emory University in partial fulfillment
of the requirements of the degree of
Bachelor of Sciences with Honors

Department of Mathematics and Computer Science

2017

Acknowledgement

I wholeheartedly thank

Alessandro Veneziani for his expertise
and his guidance through my work,

Lars Ruthotto and Michael Page for encouraging me
and serving on my thesis committee,

Alex Viguerie for his experience in FreeFem++
and generously sharing his Picard iteration solver,

Letian Wang for his inputs and help with the Latex template.

Table of Contents

Chapter 1 *Introduction*

1.1 Background and Motivation

Atherosclerotic coronary artery disease (CAD) is a disease in which plaque materials accumulate along the inner wall of arteries and reduce the arterial lumen area. The high incidence rate of CAD has nowadays draw much research attention to the studies of arterial stenosis. Many endeavors have been made by earlier researchers to build models on arterial stenosis and to investigate the interactions of local geometrical and morphological features and the hemodynamic factors. These studies involve clinical empirical studies, *in vivo*, *in vitro* experiments, and *in silico* medicine research, refering to the application of computational numerical simulations in medicine. In general, although the genesis of arterial stenosis is not yet fully understood, researchers have shown that once a stenosis has developed, it leads to irregularities in critical hemodynamic factors, such as wall-shear stress, pressure drop, separation of flow and turbulent flow [17]. Moreover, there may be a "coupling" effect between the further development stenosis and the changed flow characteristics [16]. Consequently, changes in certain local hemodynamic factors, such as reduction in maximal coronary flow level, has been proposed and are used in practice as indicators to assess the significance of stenosis [10].

On the other hand, medical image registration and fusion for the heart present special difficulties due to the beating movement and the heart's non-solid property [13].

As a result, the three-dimensional reconstruction of stenosis and the information on symmetricity of stenosis geometry are not directly available to physicians. This thesis, following up some earlier experimental work by Young [17], tries to answer the question using computational fluid dynamics analysis that *how informative blood pressure reduction over the stenosis can be in indicating the geometrical features, especially the axial symmetricity of stenoses.*

1.2 Related work

The relationship between blood pressure gradient over stenosis and the stenosis geometry has been studied by many using mathematical modeling [2, 4, 7, 15] and experimental methods [9, 17]. These works have tested on different types of axisymmetric stenosis geometries, including the ones with smooth surfaces, with irregular or jagged surfaces, and geometries whose deepest points are not in the centers of the stenosis segments. However, only few have taken into account the nonsymmetric, or eccentric stenosis geometry, in which the stenosis only concentrates on one side of the arterial wall.

In particular, the pressure-flow relationship of axisymmetric and nonsymmetric stenoses was investigated by Logan [9] through experiments on coronary arteries dissected from fresh post mortem adult hearts, Wong et al. [15] through mathematical modeling, and Young and Tsai [17] through *in vitro* experiments on a recirculating system. These studies indicate a larger pressure drop for nonsymmetric stenosis. Wong et al. [15] in 1984 tried to give a quantitative assessment based on oversimplified mathematical models to compensate for the absence of numerical methods and computational tools. This thesis, however, will give a quantitative analysis through three-dimensional

computational fluid dynamics, following the work done by Young and Tsai [17] in terms of data measurement and analysis.

1.3 Outline of the thesis

In Chapter 2, we introduce the basic physical formulations that governs the blood flow and the three-dimensional Navier-Stokes equations, followed by a discussion on numerical methods used to solve the steady Navier-Stokes system in Chapter 3. In Chapter 4, we introduce our computational fluid dynamics simulations, and the results are then presented in Chapter 5. Lastly we provide some future research directions and possible medical applications.

Chapter 2 *The 3-D Navier-Stokes Equations*

The steady, time-independent Navier-Stokes equations governs the fluid system examined in this thesis. In this chapter, we start from the general unsteady, time-dependent system, and then discuss the steadiness assumption and the governing steady Navier-Stokes equations.

2.1 Navier-Stokes problem at a glance

In general, the three-dimensional Navier-Stokes equations (2.1)-(2.2) are an expression of the conservation laws of momentum and mass for a continuous distribution of matter in the fluid state, based on the incompressible, Newtonian and homogeneous assumptions on the blood fluid

$$\frac{\partial \mathbf{u}}{\partial t} - \nu \Delta \mathbf{u} + (\mathbf{u} \cdot \nabla)\mathbf{u} + \nabla p = \boldsymbol{f} \qquad \text{in } \Omega \tag{2.1}$$

$$\nabla \cdot \mathbf{u} = 0 \qquad \text{in } \Omega \tag{2.2}$$

In this system, the independent variables are the spacial position $\mathbf{x} \in \boldsymbol{R}^3$ and time t, and dependent variables are the velocity vector field $\mathbf{u}(\mathbf{x}, t)$ and the pressure scalar field $p(\mathbf{x}, t)$. ν is a viscosity constant that we will define later. $\boldsymbol{f}(\mathbf{x}, t)$ is a forcing term given by the possible external forces. Ω is the domain of interest, which can be dependent on time, but in this thesis we consider only stationary domains. $\Delta \mathbf{u}$ is the Laplacian operator, equivalent to $\nabla \cot \nabla \mathbf{u}$, the divergence of gradient of $\mathbf{u}$. In three-dimensional

Cartesian coordinate system, the velocity $\mathbf{u} \in \mathbf{R}^3$ is a vector of three components, and (2.1) is essentially three scalar-valued differential equations: for $i = 1, 2, 3$

$$\frac{\partial u_i}{\partial t} - \nu \left(\frac{\partial^2 u_i}{\partial x_1^2} + \frac{\partial^2 u_i}{\partial x_2^2} + \frac{\partial^2 u_i}{\partial x_3^2} \right) + \left(u_1 \frac{\partial u_i}{\partial x_1} + u_2 \frac{\partial u_i}{\partial x_2} + u_3 \frac{\partial u_i}{\partial x_3} \right) + \frac{\partial p}{\partial x_i} = f_i \qquad (2.3)$$

In this section, we apply physical laws to describe the internal action of the fluid and derive the time-dependent Navier-Stokes equations. Again, the general assumptions on the blood fluid are: incompressible, homogeneous, isothermal and Newtonian. These, expressed by physical relations, are equivalent to say that the density and viscosity of the fluid do not change over time.

2.1.1 Preliminary theorems

First we introduce the the Reynolds Transport Theorem. Let $\boldsymbol{B}(\mathbf{x}, t)$ be a space-time-dependent extensive property differentiable on the bounded region Ω. $\boldsymbol{B}$ can be a scalar, vector, or a tensor. To keep it short, extensive and intensive describe how the property of a system change with the extent of the system, and the ratio of two extensive properties is an intensive property. Let m be the mass and ρ be the mass density in Ω. Define $\boldsymbol{\beta} = \boldsymbol{B}/m$, an intensive property comparable to $\boldsymbol{B}$. With a stationary, time independent Ω, Reynolds Transport Theorem states that the total change of $\boldsymbol{B}$ in time within Ω is given by

$$\frac{D\boldsymbol{B}}{Dt} = \frac{d}{dt} \int_\Omega \boldsymbol{\beta} \rho \, d\omega = \int_\Omega \frac{\partial \rho \boldsymbol{\beta}}{\partial t} \, d\omega + \int_{\partial\Omega} (\rho \boldsymbol{\beta}) \mathbf{u} \cdot \boldsymbol{n} \, dA \qquad (2.4)$$

Additionally, the Divergence Theorem states that outward flux of a vector field through a closed surface is equal to the volume integral of the divergence over the region inside the surface

$$\int_{\partial\Omega} \boldsymbol{F} \cdot \boldsymbol{n} \, dA = \int_\Omega \nabla \cdot \boldsymbol{F} \, d\omega. \qquad (2.5)$$

Equipped with these theorems, we can now consider the two principal conservation laws on mass and momentum, and apply some constitutive laws to obtain the general Navier-Stokes equations.

2.1.2 Conservation of mass

The conservation law of mass states that $\frac{\partial m}{\partial t} = 0$, despite the change in mass volume or density. Apply Reynold's Theorem (2.4) taking $B = m$, $\beta = 1$, we have

$$\begin{aligned} \frac{dm}{dt} = \frac{d}{dt}\int_\Omega \rho \, d\omega &= \int_\Omega \frac{\partial \rho}{\partial t} \, d\omega + \int_{\partial\Omega} \rho \mathbf{u} \cdot \boldsymbol{n} dA. \\ &= \int_\Omega \frac{\partial \rho}{\partial t} \, d\omega + \int_\Omega \nabla \cdot (\rho \mathbf{u}) \, d\omega = 0 \end{aligned} \tag{2.6}$$

Because the choice of Ω is arbitrary, (2.6) must hold for all regions that the fluid goes through. We then arrive at the strong form of conservation of mass

$$\frac{\partial \rho}{\partial t} + \nabla \cdot (\rho \mathbf{u}) = 0. \tag{2.7}$$

As we assume the blood fluid is incompressible and isothermal, $\partial\rho/\partial t = 0$. (2.7) gives the incompressibility constraint in Navier-Stokes equations: $\nabla \cdot \mathbf{u} = 0$.

2.1.3 Conservation of momentum

For any fluid element, the only forces exerted on it are the volumic and surface forces. The volumic forces refer to the gravity force and other forces exerted to the fluid from external. The surface forces refer to the forces due to the stress tensor. According to Newton's second law,

$$\boldsymbol{F}_{net} = \frac{d(m\mathbf{u})}{dt} = \boldsymbol{f}_v + \boldsymbol{f}_s. \tag{2.8}$$

Apply Reynold's Transport Theorem with $\boldsymbol{B} = m\mathbf{u}$, $\beta = \mathbf{u}$,

$$\begin{aligned}\frac{d(m\mathbf{u})}{dt} = \frac{d}{dt}\int_\Omega \rho\mathbf{u}\, d\omega &= \int_\Omega \frac{\partial(\rho\mathbf{u})}{\partial t}\, d\omega + \int_{\partial\Omega} \rho\mathbf{u}(\mathbf{u}\cdot\boldsymbol{n})\, dA \\ &= \int_\Omega \left(\frac{\partial(\rho\mathbf{u})}{\partial t} + \nabla\cdot(\rho\mathbf{u}\mathbf{u})\right)\, d\omega. \end{aligned} \tag{2.9}$$

In (2.9), $\mathbf{u}\mathbf{u}$ is defined as a matrix with the (i,j) term being $u_i u_j$. Also notice that,

$$\begin{aligned}\frac{\partial(\rho\mathbf{u})}{\partial t} + \nabla\cdot(\rho\mathbf{u}\mathbf{u}) &= \left[\frac{\partial\rho}{\partial t}\mathbf{u} + \rho\frac{\partial\mathbf{u}}{\partial t}\right] + [\nabla\cdot(\rho\mathbf{u})\mathbf{u} + \rho\mathbf{u}\cdot\nabla\mathbf{u}] \\ &= \underbrace{\left(\frac{\partial\rho}{\partial t} + \nabla\cdot(\rho\mathbf{u})\right)\mathbf{u}}_{=0 \text{ due to mass conservation (2.7)}} + \rho\left(\frac{\partial\mathbf{u}}{\partial t} + (\mathbf{u}\cdot\nabla)\mathbf{u}\right) \end{aligned} \tag{2.10}$$

Therefore,

$$\frac{d(m\mathbf{u})}{dt} = \rho\int_\Omega \left(\frac{\partial\mathbf{u}}{\partial t} + (\mathbf{u}\cdot\nabla)\mathbf{u}\right)\, d\omega = \boldsymbol{f}_v + \boldsymbol{f}_s. \tag{2.11}$$

Consider the mass gravity and no other external forces, and the volumic force

$$\boldsymbol{f}_v = m\boldsymbol{g} = \int_\Omega \rho\boldsymbol{g}\, d\omega. \tag{2.12}$$

As with surface forces, the stress tensor $\mathbf{S}$ experienced by the fluid is, by constitutive laws, a three-by-three matrix given by

$$\boldsymbol{S} = -\boldsymbol{I}\left(p + \lambda\underbrace{\nabla\cdot\mathbf{u}}_{=\mathbf{0}}\right) + \mu(\nabla\mathbf{u} + \nabla\mathbf{u}^T) \tag{2.13}$$

where $\boldsymbol{I}$ is an identity matrix, λ and μ are scalar viscosity coefficients found in empirical experiments. Then $\boldsymbol{S} = -\boldsymbol{I}p + \mu\nabla\mathbf{u}$, and the surface force

$$\begin{aligned}\boldsymbol{f}_s &= \int_{\partial\Omega} \boldsymbol{S}\cdot\boldsymbol{n}\, dA = \int_\Omega \nabla\cdot\boldsymbol{S}\, d\omega \\ &= \int_\Omega -\nabla p + \mu\nabla\cdot(\nabla\mathbf{u} + \nabla\mathbf{u}^T)\, d\omega \end{aligned} \tag{2.14}$$

In particular, denote $\frac{\partial}{\partial x_a}(\frac{\partial}{\partial x_b}) = \partial^2_{ab} u_1$, $\nabla \mathbf{u}^T$ can be written such that

$$\nabla \cdot \nabla \mathbf{u}^T = \begin{bmatrix} \partial^2_{11} u_1 + \partial^2_{21} u_2 + \partial^2_{31} u_3 \\ \partial^2_{12} u_1 + \partial^2_{22} u_2 + \partial^2_{32} u_3 \\ \partial^2_{13} u_1 + \partial^2_{23} u_2 + \partial^2_{33} u_3 \end{bmatrix} = \sum_{i=1,2,3} \mathbf{e}_i \left(\partial^2_{1i} u_1 + \partial^2_{2i} u_2 + \partial^2_{3i} u_3 \right)$$

Assume that $\mathbf{u}$ has continuous second order derivatives, then the second order partial derivatives are invertible and we have

$$\nabla \cdot \nabla \mathbf{u}^T = \sum_{i=1,2,3} \mathbf{e}_i \partial_i \left(\partial_1 u_1 + \partial_2 u_2 + \partial_3 u_3 \right) = \sum_{i=1,2,3} \mathbf{e}_i \partial_i \left(\nabla \cdot \mathbf{u} \right).$$

As we have the incompressibility constraint, $\nabla \cdot \nabla \mathbf{u}^T$ vanishes and

$$\boldsymbol{f}_s = \int_\Omega -\nabla p + \mu \nabla \cdot \nabla \mathbf{u} \, d\omega. \tag{2.15}$$

Combining the forces (2.12), (2.15) with the conservation law of momentum (2.11), we have

$$\frac{\partial \mathbf{u}}{\partial t} + \mathbf{u} \cdot \nabla \mathbf{u} = -\frac{1}{\rho} \nabla p + \frac{\mu}{\rho} \Delta \mathbf{u} + \boldsymbol{g} \tag{2.16}$$

After nondimensionalization and introducing $\nu = \mu / \rho$, the kinematic viscosity into this equations, (2.1) is obtained: $\frac{\partial \mathbf{u}}{\partial t} - \nu \Delta \mathbf{u} + (\mathbf{u} \cdot \nabla) \mathbf{u} + \nabla p = \boldsymbol{f}$.

2.2 Steady Navier-Stokes equations

In this thesis, we assume that the blood flow through the domain of interest is independent of time, and the fluid properties depend only on its position $\mathbf{x}$ relative to Ω. The governing equations of our problem are thus time-independent. Dropping the velocity-time derivative term in (2.1), we seek to solve the steady Navier-Stokes equations

$$-\nu \Delta \mathbf{u} + (\mathbf{u} \cdot \nabla) \mathbf{u} + \nabla p = \boldsymbol{f} \qquad \text{in } \Omega \tag{2.17}$$

$$\nabla \cdot \mathbf{u} = 0 \qquad \text{in } \Omega, \tag{2.18}$$

The assumption of steadiness is clearly a strong simplification, as the circulation is obviously a time-dependent problem. However, for this preliminary assessment, and following the work in [17], the steady assumption is just a first step that eventually will be followed up by further numerical investigations in unsteady regime. It is also worth noting that in most of the cases, doctors refer to time averaged informations. In other terms, the synthesis of a numerical simulation often is given by the time average of an unsteady simulation. Steady models may surrogate the process of time averaging of an unsteady simulation, with a significant improvement of the computational efficiency. This is a subject of current research in the group of the Emory Biomech Core Lab.

Chapter 3 *Numerical Approaches*

In this chapter, we introduce the numerical methods applied to solve the steady Navier-Stokes system. We first formulate the weak form of the equations, and then discretize it using Finite Element method. Ending up with a nonlinear finite-dimensional system, we apply Picard iteration to linearize the system and to solve it numerically.

3.1 The Weak Formulation

For the sake of simplicity, we keep a general zero Dirichlet conditions for the steady Navier-Stokes equations (2.17)-(2.18)

$$\mathbf{u}(\Gamma_D) = 0 \text{ on } \Gamma_D = \partial\Omega.$$

Other case-specific boundary conditions are illustrated later in section 4.2. Moreover, if a nonzero Dirichlet boundary condition is imposed, we then introduce a lifting function and it is eventually be taken care of by the forcing term. A general analysis on the existence and uniqueness of solution for Navier Stokes equations under Dirichlet and Neumann boundary conditions can be found in [11]. The forcing term is usually taken as $\mathbf{f} = \mathbf{0}$ since the only external force applied to the blood flow is the body gravity. In general, gravity has a minor impact on blood in coronary arteries and it can be incorporated in the pressure [3].

Let $V = H_0^1(\Omega)$, $Q = L^2(\Omega)$. $L^2(\Omega)$ denotes the Lebesgue space and $H_0^1(\Omega)$, the Soblev space of functions defined on Ω, vanishing on the boundary and whose up to

second order weak derivatives are in $L^2(\Omega)$. Take test functions $\mathbf{v} \in V$ and $q \in Q$, corresponding to the function spaces of velocity $\mathbf{u}$ and the pressure p. Notice that $\mathbf{v} = 0$ on the boundary Γ_D. Multiply (2.17) by $\mathbf{v}$ and (2.18) by q, and then integrate by part the first and third terms in (2.17), we obtain the formulation of weak derivatives

$$\nu \int_\Omega \nabla \mathbf{u} : \nabla \mathbf{v} + \int_\Omega ((\mathbf{u} \cdot \nabla)\mathbf{u})\mathbf{v} - \int_\Omega p(\nabla \cdot \mathbf{v}) = \int_\Omega \boldsymbol{f}\mathbf{v} \tag{3.1}$$

$$\int_\Omega (\nabla \cdot \mathbf{u})q = 0 \tag{3.2}$$

All terms integrated on the boundary resulting from the by-part integration are eliminated by the zero Dirichlet boundary condition.Then the problem reads:

Find $\mathbf{u} \in V$ and $p \in Q$ such that (3.1)-(3.2) is true for all $\mathbf{v} \in V$ and $q \in Q$.

From (2.17)-(2.18) to (3.1)-(3.2), we reformulate the second order derivative term on $\mathbf{u}$ and the first order derivative of p. The weak formulation allows solutions with less regularities than the strong form requires. But it is still a correct representation of the problem for functions attaining regularity of those involved in the physical problem and the definition of the differential operations involved.

3.2 Finite Element Approximation

Having obtained the weak formulation, the numerical solution of this problem still requires that we translate it into a finite dimensional numerical problem.

We first subdivide the three-dimensional domain Ω into meshes. Denote by h the maximum size of the mesh elements. Finite Element method assumes that our solutions $\mathbf{u}$ on every mesh element can be approximated by the linear combination of a set of selected linearly independent functions that we refer to as "basis functions" $\{\boldsymbol{\varphi}_i\}$. In

other words,

$$\mathbf{u} \cong \mathbf{u}_h = \sum_{1 \le i \le 3N_u} u_i \boldsymbol{\varphi}_i(\mathbf{x}), \tag{3.3}$$

where N_u, referred to as the degree of freedom, is the number of linearly independent space basis functions we have in one space dimension. Generally the degree of freedom is inversely related to h. These basis functions are selected so that the space spanned by them V_h, is a finite dimensional subspace of the function spaces V. Similarly, we select $\{\psi_j\}$ to approximate the pressure $p \cong p_h = \sum_{1 \le i \le N_p} p_j \psi_j(\mathbf{x})$ where N_p is the degree of freedom of the discrete pressure space. Now we want to take test functions $\mathbf{v}_h \in V_h$ and $q_h \in Q_h$, substitute $\mathbf{u}_h$ and p_h into the weak form (3.1)-(3.2), and the discrete problem reads:

Find $\mathbf{u}_h \in V_h$ and $p_h \in Q_h$ such that the following equations hold for all $\mathbf{v}_h \in V_h$ and $q_h \in Q_h$

$$\nu \int_\Omega \nabla \mathbf{u}_h : \nabla \mathbf{v}_h + \int_\Omega (\mathbf{u}_h \cdot \nabla \mathbf{u}_h)\mathbf{v}_h - \int_\Omega p_h (\nabla \cdot \mathbf{v}_h) = \int_\Omega \boldsymbol{f} \mathbf{v}_h \tag{3.4}$$

$$\int_\Omega q_h (\nabla \cdot \mathbf{u}_h) = 0. \tag{3.5}$$

This representation, where the solutions of the problem are approximated by linear combinations of basis functions and substituted into the original problem is called *Galerkin approach*. In particular, with Finite Elements, the basis functions are piecewise polynomials.

Notice that these relations hold for all test functions $\mathbf{v}_h \in V_h$ if and only if they hold for all velocity basis functions $\boldsymbol{\varphi}_i(\mathbf{x})$. So are for q_h and ψ_j. So if we denote $\boldsymbol{u} = (u_1, ..., u_{3N_u})$ and $\boldsymbol{p} = (p_1, ..., p_{N_p})$ and rearrange the system, we obtain the following matrix form

$$\begin{bmatrix} K + N(\boldsymbol{u}) & B^T \\ B & 0 \end{bmatrix} \begin{bmatrix} \boldsymbol{u} \\ \boldsymbol{p} \end{bmatrix} = \begin{bmatrix} \boldsymbol{f} \\ \boldsymbol{0} \end{bmatrix}, \tag{3.6}$$

where K corresponds to the diffusive term and $N(\boldsymbol{u})$ corresponds to the nonlinear convective term.

The nonlinearity comes from the nonlinear convective term. In absence of this term, we obtain a linear system. Unfortunately, the nonsingularity of this system is not immediate. In fact, it was proven by the Italian mathematician Franco Brezzi that the nonsingularity of the system is guaranteed only if the discrete spaces V_h and Q_h are properly chosen. Specifically, a condition known as Ladyzhenskaya-Babuska-Breezi must be enforced. As an instance, the combination of piecewise linear functions for both velocity and pressure is not LBB compatible. On the contrary, piecewise quadratic functions for the velocity and piecewise linear functions for the pressure fulfill the compatibility condition. This choice has a drawback of requiring many degrees of freedom for the velocity and eventually of leading to large (sparse) linear systems to solve. Clearly, this has an impact on the computational costs. In this work, we use exactly piecewise quadratic velocities and piecewise linear pressures. Other choices are possible, we select this one because it is well rooted in the theory of finite elements and, in particular, the accuracy properties of this choice are well known and verified.

The numerical solution of the problem requires now to manage nonlinearity. There are several methods for finding the solution of nonlinear algebraic systems, including the Newton method that resorts to the construction of the Jacobian matrix associated with the problem. Even if this method generally guarantees excellent convergence rate, it requires the explicit computation of the derivatives of the nonlinear functions. Also, the convergence is guaranteed only if the initial guess is close enough to the exact solution.

We refer to [8] for a complete analysis of the Newton method for the incompressible Navier-Stokes equations. Here, we prefer to use a more robust method, called Picard iterations. In fact, this method is generally slower, but the pool of initial guesses that guarantee convergence is generally much wider than for the Newton one (see [8] for details). We illustrate the Picard method in the next Section.

3.3 Linearization: Picard Iteration

Picard iteration starts from an initial guess $[\mathbf{u}^{(0)}, p^{(0)}]^T$. At each iteration, we substitute the solution from the previous step into the convective term in (2.17) to obtain an approximation $(\mathbf{u}^{(n)} \cdot \nabla)\mathbf{u}^{(n)} \approxeq (\mathbf{u}^{(n-1)} \cdot \nabla)\mathbf{u}^{(n)}$. To see this in the discretized form (3.6), taking initial guess $[\boldsymbol{u}^{(0)}, \boldsymbol{p}^{(0)}]^T$ and substituting $\boldsymbol{u}^{(n-1)}$ to $N(\boldsymbol{u})$ at each iteration, we get the following linear system

$$\begin{bmatrix} K + N(\boldsymbol{u}^{(n-1)}) & B^T \\ B & 0 \end{bmatrix} \begin{bmatrix} \boldsymbol{u} \\ \boldsymbol{p} \end{bmatrix} = \begin{bmatrix} \boldsymbol{f} \\ 0 \end{bmatrix} \tag{3.7}$$

If the initial velocity guess is taken as zero, then the first iteration is essentially the Stokes problem.

3.3.1 Incremental analysis

The iteration stops when a certain level of convergence is approached. We consider the L^2 norm of increment in velocity $\delta\mathbf{u}^{(n)}$ at each iteration n as a convergence criteria. The increment is defined as $\mathbf{u}^{(n)} - \mathbf{u}^{(n-1)}$ and the L^2 norm is

$$\delta\mathbf{u}^{(n)} = \|\mathbf{u}^{(n)} - \mathbf{u}^{(n-1)}\|_{L^2(\Omega)} = \sqrt{\int_\Omega (\mathbf{u}^{(n)} - \mathbf{u}^{(n-1)})^2 \; d\omega}.$$

If $\delta\mathbf{u}^{(n)}$ is smaller than some pre-determined tolerance value, we say the Picard iteration converges and stop the loop.

3.3.2 Relaxation

For the purpose of enhancing the convergence of the iterative method, we introduced a relaxation parameter γ when updating the new solution [14]. Denote the velocity field solution of Picard iteration n by $\hat{\mathbf{u}}^{(n)}$. Instead of updating the system with $\hat{\mathbf{u}}^{(n)}$, we compute

$$\mathbf{u}^{(n)} = \gamma\hat{\mathbf{u}}^{(n)} + (1-\gamma)\mathbf{u}^{(n-1)}$$

where $\gamma \in (0, 1]$ and substitute $\mathbf{u}^{(n)}$ into the convective term. With $\gamma = 1$, we have the original unrelaxed version of Picard iteration. In general, a smaller $\gamma \in (0, 1)$ reduces the rate of convergence and requires more iterations to obtain convergence, but will guarantee better convergent performance. See [14] for the analysis on the choices of γ.

Chapter 4 *Modeling and CFD Simulations*

4.1 Stenosis geometries

We prepared three-dimensional axisymmetric and nonsymmetric stenosis geometries (Figure 4.1) as the region for the computational fluid dynamics (CFD) simulations. The stenosis in blood vessels are modeled by the constricted portions in cylindrical tubes. Both axisymmetric and nonsymmetric ASCII `STL` surface meshes are first generated with MATLAB scripts. Due to geometrical irregularities, the nonsymmetric geometries are put to cleaning and repairing in `MeshLab`, an open source system for processing and editing 3D triangular meshes [5]. Finally `Netgen` is utilized to generate `Gmesh2` volume tetrahedron mesh, which could be fed to simulations in `FreeFem++`.

4.1.1 Geometry description

The axisymmetric geometry considered here has the same commonly used shape as introduced in [17]. The radius r of the cross-section circle is described as a cosine function of the z coordinate:

$$r(z) = R_0 - \frac{\delta}{2}\left(1 + \cos\frac{\pi z}{Z_0}\right), \quad -Z_0 \le z \le Z_0 \tag{4.1}$$

and $r(z) = R_0$ otherwise. Here R_0 is the radius of the unrestricted part of the tube, Z_0 is half of the total length of constriction, and $0 \le \delta < R_0$ is the maximal depth of constriction, as shown in Figure 4.1a.

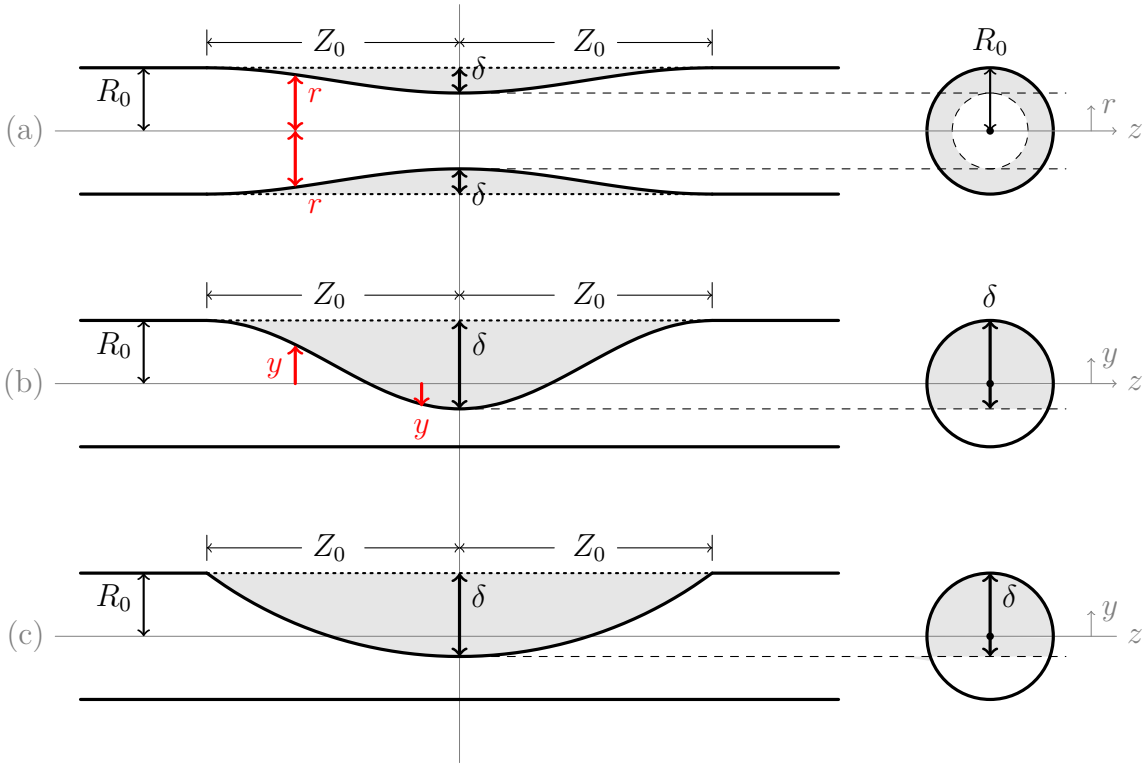

Figure 4.1: The profiles of stenosis geometries. (a): Axisymmetric shape used in this thesis and Young and Tsai's experiments [17]; (b): Nonsymmetric shape used in this thesis; (c): Nonsymmetric shape used in Young and Tsai experiments.

Figure 4.1c shows the nonsymmetric stenosis geometry implemented by Young and Tsai[17], where the boundary of constricted portion y is given by a circular arc rather than a cosine function. This geometry often will introduce instability in CFD results, due to the fact that the sharp angle formed by the circular arc and the tube wall is in the direction of fluid inflow. Therefore we smooth the profile into a cosine shape. The nonsymmetric geometry examined in this thesis is described in Figure 4.1b, where the depth of constriction y is given by a similar cosine function as (4.1) $y(z) = R_0 - \frac{\delta}{2}\left(1 + \cos\frac{\pi z}{Z_0}\right)$, with $-Z_0 \leq z \leq Z_0$. Notice that now for nonsymmetric geometries, restrictions are set on y (see Figure 4.1b), the Cartesian coordinates of surface points, rather than the radius r. In addition, the maximal depth of constriction has a different range $0 \leq \delta < 2R_0$.

Table 1 summarizes some related geometrical characteristics of the stenosis geometries used in the test simulation. In all models, we fix the normal radius $R_0 = 0.5$, half stenosis length $Z_0 = 2$. If we define $A_0 = \pi R_0^2$ as the cross-section area of the unrestricted tube, and write the cross-sectional area A as a function of z, then area reduction $\Delta_A = A(0)/A_0$, and volume reduction $\Delta_V = \int_{-Z_0}^{Z_0} A(z)\, dz/2A_0Z_0$. As shown in the table, under same area reduction, the two types of geometries do not differentiate too much in volume reduction.

Model No.	%Area Reduction (Δ_A)	δ	δ/R_0	%Volume Reduction (Δ_V)
S1	20	0.0528	10.56%	10.14
S2	40	0.1127	22.54%	20.63
S3	60	0.1838	36.76%	31.69
N1	20	0.2541	50.82%	8.11
N2	40	0.4211	84.22%	17.05
N3	60	0.5789	115.78%	26.25

Table 1. *Stenosis Geometry. For Model Numbers, S denotes axisymmetric stenosis geometries, and N denotes nonsymmetric stenosis geometries.*

4.1.2 Construction and meshing

In this section, we briefly explain the construction of our ASCII `STL` surface mesh. ASCII `STL` files store the geometry as a collection of triangles, and triangles as a structured collection of norms and vertices. We take advantage of this structure and the idea of cylindrical coordinate system to construct the geometry surfaces. The basic idea is to subdivide 2π into grids of size $d\theta$ and then "rotate" the cosine function 4.1 around the central axis by step $d\theta$. The algorithm keeps track of a set of points $(P(i,j,1), P(i,j,2), P(i,j,3))$, where i, j indicates the cylindrical position of the "rotation", and $P(i,j,1)$, $P(i,j,2)$, $P(i,j,3)$ are the x, y, z coordinates of the points:

while $i < Z_0/dz$ **do**
  while $j < 2\pi/d\theta$ **do**
    Make triangle: $(r(z_i), \theta_j, z_i)$, $(r(z_i), \theta_{j+1}, z_i)$,$(r(z_{i+1}), \theta_j, z_{i+1})$;
    Make triangle: $(r(z_i), \theta_j, z_i)$, $(r(z_{i+1}), \theta_{j+1}, z_{i+1})$,$(r(z_{i+1}), \theta_j, z_{i+1})$;
  end
end

Algorithm 1

In general, all stenosis geometries used in this thesis are generated with $dz = 0.04$ and 200 linear spaced grids on radial direction so that the surface mesh is sufficiently regular, as shown in Figure 4.2.

For the nonsymmetric stenosis geometry, at each z value, the stenotic portion is divide by equally spaced nodes, and then triangles are constructed accordingly, as illustrated in Figure 4.3a. At the cornersof the stenosis, nodes on the stenotic surface may become too close to node on the regular surface, leading to long sharp triangles and singularities (Figure 4.3b). We then fix the geometries with `MeshLab` [5]. The corrected geometry is as shown in Figure 4.4.

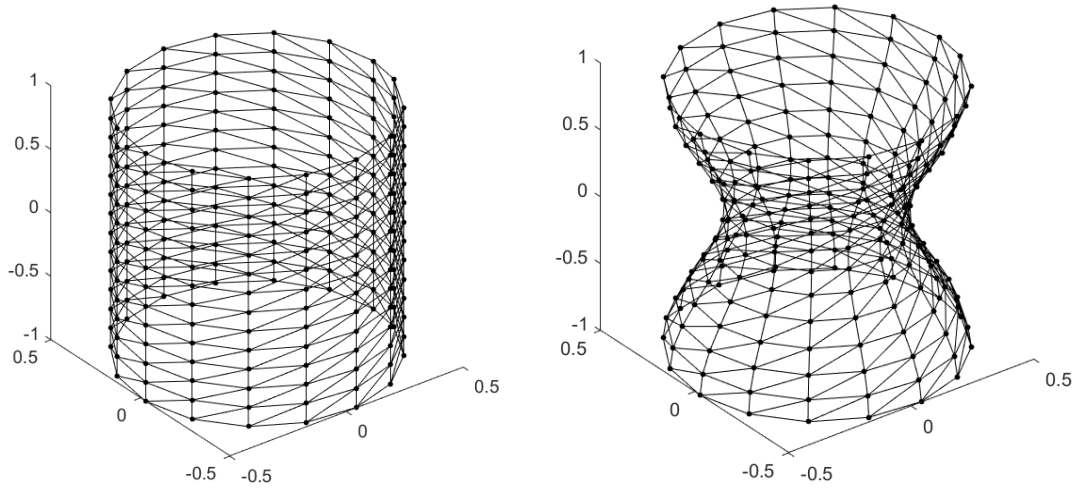

(a) (b)

Figure 4.2: Surface triangular meshes constructed using Algorithm 1 (not in scale with the ones used for simulation). (a): without any stenosis; (b): with symmetric stenosis, by shrinking the radius according to Equation (4.1).

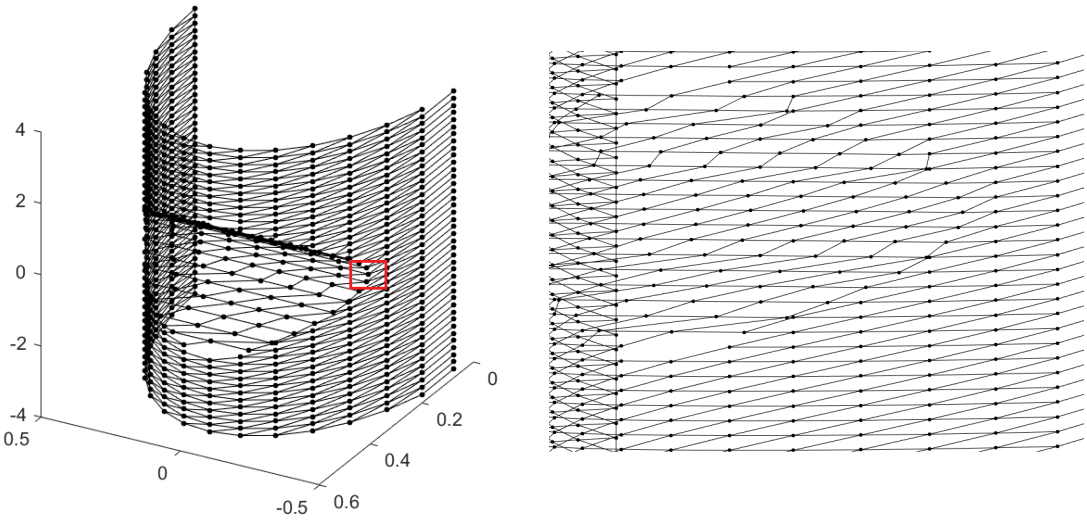

(a) (b)

Figure 4.3: Illustration of surface triangular meshes for nonsymmetric stenosis. (b) is a close-up view of the portion in (a) enclosed by the rectangular. Notice the bad triangles and possible singularities caused by two nodes that are too close to each other. This occurs at the edge of the stenosis.

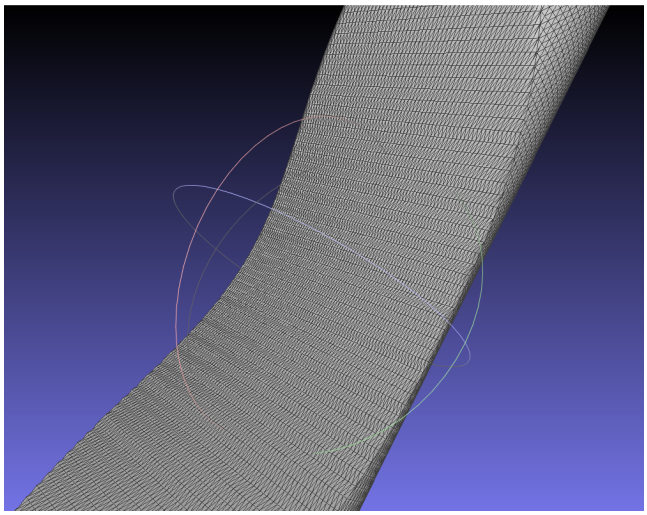

Figure 4.4: The nonsymmetric stenosis repaired by `MeshLab`, percentage area stenosis = 0.6.

4.2 Boundary conditions

The imposition of suitable boundary conditions on is essential for the problem to be well posed. In this section, we introduce the boundary conditions enforced in our simulations. Denote the boundaries surfaces as $\Gamma = \partial\Omega = \Gamma_{in} + \Gamma_{out} + \Gamma_{wall}$.

In general, we have Dirichlet conditions for velocity on Γ_{wall} and Γ_{in}. We assume that the vessel wall is not moving or interacting with the fluid, and enforce on Γ_{wall} the so-called no-slip zero velocity condition. This means that $\mathbf{u} = \mathbf{0}$ On Γ_{wall}, we characterize a constant parabolic inflow with maximal inflow in the center and zero on the edge. Placing the central axis of the tube on z axis, the inflow velocity can be written explicitly as

$$u_x = 0,\ u_y = 0,\ u_z = U_{in}(1 - \frac{x^2 + y^2}{R_0^2}) \tag{4.2}$$

The total inflow is given by $Q_{in} = \int_{\Gamma_{in}} \mathbf{u} \cdot \boldsymbol{n}\ d\omega$.

In order to impose proper values of U_{in} for simulation, let us define Reynolds number

as

$$Re = \frac{\rho U R}{\mu} = \frac{U R}{\nu}$$

where U is the characteristic inflow velocity that we will impose in (4.2), ν the kinematic viscosity as in the Navier-Stokes equations, R is the characteristic length, taken in this case as the diameter of the unrestricted tube. Note that Reynolds number is inversely proportional to ν, and ν governs the diffusive term in the Navier-Stokes equations (2.17). Reynolds numbers is thus a measure of how the convective term dominates the diffusive one in our system [11]. In fact, larger Reynolds numbers often indicate disturbed or even turbulent flow. But in general, blood flow is non-turbulent, and in this thesis, we simulated with mild Reynolds numbers 200, 300, 400, 500 and 700.

For Γ_{out}, we impose a Neumann condition on pressure, also known as the "standard do-nothing approach", as is introduced in [12]

$$p\boldsymbol{n} - \nu \nabla \mathbf{u} \cdot \boldsymbol{n}|_{\Gamma_{out}} = \mathrm{P}_{distal}\boldsymbol{n}. \tag{4.3}$$

where P_{distal} is a scalar "standard" blood pressure value we want to enforce on the outlet. Recall in section 3.1, we apply integration by part to the first and third terms in (2.17) to derive the weak formulation with zero Dirichlet boundary conditions. Now we reproduce the by-part integration, taking account of the Neumann condition, and we get

$$\begin{aligned} -\nu \int_\Omega \Delta \mathbf{u} \cdot \mathbf{v} + \int_\Omega \nabla p \cdot \mathbf{v} &= -\nu \left(\int_\Gamma (\nabla \mathbf{u} \cdot \boldsymbol{n}) \mathbf{v} - \int_\Omega \nabla \mathbf{u} : \nabla \mathbf{v} \right) + \int_\Gamma p\boldsymbol{n} \cdot \mathbf{v} - \int_\Omega p(\nabla \cdot \mathbf{v}) \\ &= \underbrace{\int_\Gamma (p\boldsymbol{n} - \nu \nabla \mathbf{u} \cdot \boldsymbol{n}) \cdot \mathbf{v}}_{(\star)} + \int_\Omega \nabla \mathbf{u} : \nabla \mathbf{v} - \int_\Omega p(\nabla \cdot \mathbf{v}) \end{aligned} \tag{4.4}$$

Notice that $\mathbf{v} = \mathbf{0}$ Dirichlet conditioned boundaries, so $(\star)$ vanishes on Γ_{in} and Γ_{wall}. $p\boldsymbol{n} - \nu \nabla \mathbf{u} \cdot \boldsymbol{n} = \mathrm{P}_{distal} \cdot \boldsymbol{n}$ on Γ_{out}, then the term $(\star)$ adds a nonzero term integrated

on Γ_{out} to the left hand side of (3.1), and gives a new weak formulation:

$$\nu \int_{\Omega} \nabla \mathbf{u} : \nabla \mathbf{v} + \int_{\Omega} ((\mathbf{u} \cdot \nabla)\mathbf{u})\mathbf{v} - \int_{\Omega} p(\nabla \cdot \mathbf{v}) + \int_{\Gamma_{out}} \mathrm{P}_{distal} \boldsymbol{n} \cdot \mathbf{v} = \int_{\Omega} \boldsymbol{f} \mathbf{v} \tag{4.5}$$

4.3 Numerical solution

We simulated the previously analyzed problem on axisymmetric and nonsymmetric stenosis geometries with area reduction of 20%, 40% and 60%, under Reynolds number 200, 300, 400, 500 and 700. The computation is implemented in and solved with `FreeFem++` [6] code by Alex Viguerie [14]. The UMFPACK64 solver is used to solve the linear systems. `FreeFem++` is a C++ based software that solves two- or three-dimensional partial differential equations numerically based on Finite Element method. We use `FreeFem++` because it is free, highly adaptive and easily implemented.

The numerical solutions are exported in the format of VTK, containing the point set and the corresponding attribute data. We then use `ParaView` [1] visualize the VTK file and to extract point-wise results for further analysis.

Chapter 5 *Results, Discussion and Follow-ups*

In this chapter, we interpret and discuss the simulation results on pressure drops and pressure distributions. Comparisons are made between results of axisymmetric and of nonsymmetric stenosis geometries, as well as between simulated results of this work and Young and Tsai's experimental results [17]. Some approaches of interpretation and definitions follows [17] in their post-processing of their experimental results, as will be noted at their appearance.

5.1 Results and Discussion

Let us first introduce a dimensionless pressure reduction

$$\frac{\Delta P}{\rho U^2} = \frac{P_{upstream} - p(z)}{\rho U^2},$$

where ΔP is the pressure reduction relative to upstream, ρ the fluid density and U the characteristic velocity. This quantity is commonly used in describing the pressure drop across a restriction. We will take U as the inflow velocity (as given by Reynolds number and the geometry) and the pressure at $z/Z_0 = -4$ as the "upstream" reference pressure [17]. In the following discussion, we refer to this quantity as pressure drop. The axial position is measured accordingly by z/Z_0, the ratio of position and half stenosis length. All geometric models were constructed with axial range $-4Z_0 \leq z \leq 4Z_0$ to allow length for the pressure to recover, as noted by [17]. The segment of reduction is then $-Z_0 \leq z \leq Z_0$.

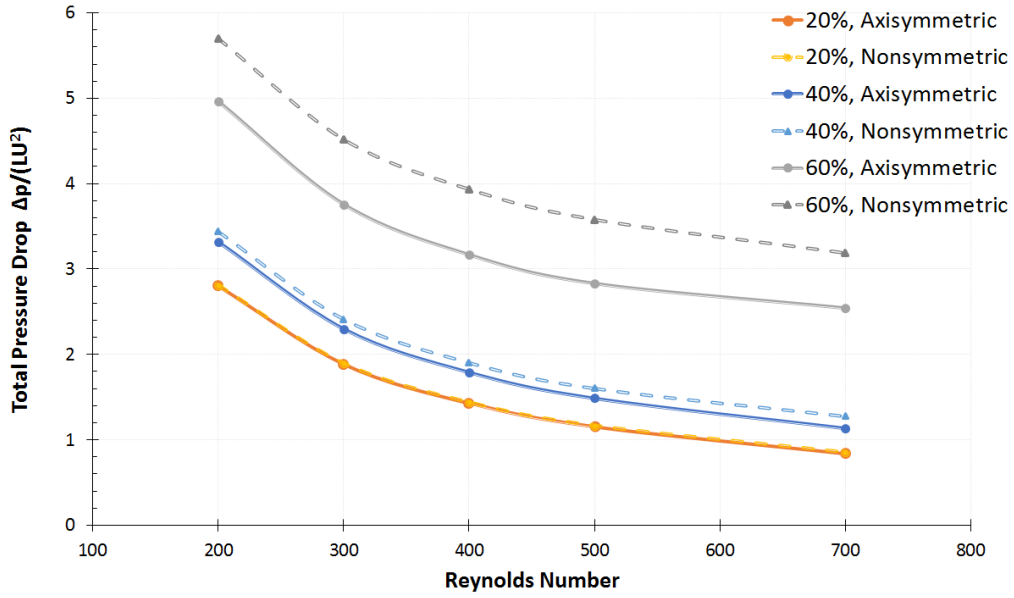

Figure 5.1: The total pressure drop from the inlet to the outlet. For comparison, models with same level of percentage area stenosis are marked in similar colors.

The total amounts of pressure drop from the inlet boundary $z/Z_0 = -4$ to the outlet boundary $z/Z_0 = 4$ for all simulated models are shown in Figure 5.1. The gaps between axisymmetric and nonsymmetric models enlarge as the percentage area stenosis grows. In fact, as the yellow curves illustrated in Figure 5.1, for insignificant stenosis like the ones with 20% area reduction, the total amount of pressure reduction does not differentiate between axisymmetric or nonsymmetric at all.

Figure 5.2 shows the pressure drop distributions along the side walls of the 20% and 60% stenosis geometry under Reynolds number 700. Similar distribution patterns are present for other models. The three curves in each figure are of the same percentage area reduction; one taken from an arbitrary side of the axisymmetric model, two others each from the stenotic and nonstenotic side walls of nonsymmetric stenosis geometries.

For axisymmetric stenoses, the pressure decreases continuously until the midpoint

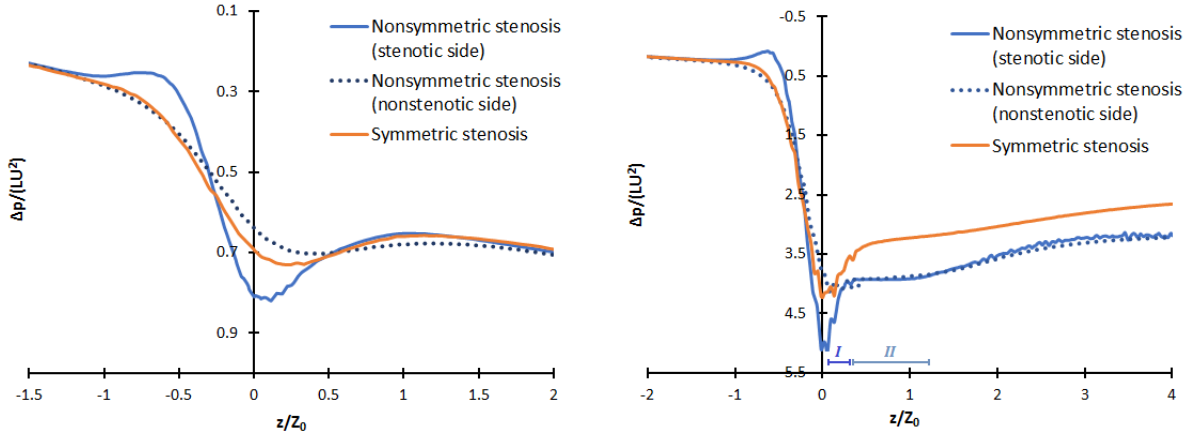

(a) (b)

Figure 5.2: Typical pressure drop distribution along the stenotic arterial walls, $Re = 700$. Only portions with significant difference are depicted for the sake of contrast and comparison; in non-shown portions, the three curves overlap. (a): 20% area reduction on $-1.5 \leq z/Z_0 \leq 2$; (b): 60% area reduction on $-2 \leq z/Z_0 \leq 4$. On (b), the two phases mentioned on page 5.1 are specified.

$z/Z_0 = 0$ is reached, and this pressure drop accelerates at around $z/Z_0 = -0.5$, shortly after reaching the constricted part. While for nonsymmetric models (without special notes, we refer to the stenotic side of the nonsymmetric model), there is a short pressure increase upon reaching the constriction at $z/Z_0 = -1$. After that, at around $z/Z_0 = -0.5$ the pressure falls sharply with a rate larger than that of axisymmetric models. The lowest pressure for both axisymmetric and nonsymmetric models occur shortly downstream the midpoint $z/Z_0 = 0$; however, nonsymmetric models induce more pressure drop over the stenosis, reaching a lower minimal point. Downstream the midpoint, the recovery of pressure for both cases can be loosely divided into a phase of sharp bounce and a relatively stable phase, as specified on Figure 5.2b. With a deeper stenosis, the division between these two phases is more distinct, and it takes much longer for the pressure to finally recover (to the natural mild-drop state).

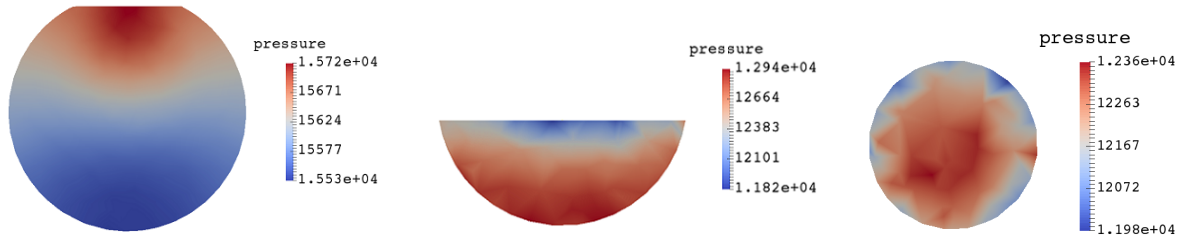

(a) (b) (c)

Figure 5.3: Cross-sectional pressure distributions for area stenosis 60% axisymmetric and nonsymmetric geometries, simulated at $Re = 700$. (a): Nonsymmetric stenosis, taken at $z/Z_0 = -0.8$; (b): Nonsymmetric stenosis, taken at the midpoint $z/Z_0 = 0$; (c): Axisymmetric stenosis, taken at the midpoint $z/Z_0 = 0$.

In addition, the cross-sectional pressure distribution (Figure 5.3a,b) taken at $z/Z_0 = -0.8$ and 0 of the nonsymmetric model shows and explains the different pressure distribution between the stenotic and nonstenotic sides. At $z/Z_0 = -0.8$, fluid pressure increases as the fluid hits forward onto the constricted stenosis; then the fluid is led by the stenosis shape towards the the other side of the tube, increasing the pressure on nonstenotic side near $z/Z_0 = 0$. On the contrary, in axisymmetric models, we always observe axisymmetric pressure distribution, as shown in Figure 5.3c.

Despite the discrepancies described above, with a negligible to mild stenosis, the downstream distinction in pressure drop is hardly measurable. The two curves (Figure 5.2a) overlap from around $z/Z_0 = 0.5$, even before the normal nonstenotic segment is reached. This observation verifies our previous finding in total pressure drop on mildly stenotic geometries. But the downstream pressures do differentiate between axisymmetric and nonsymmetric models in more severe stenosis models (both 40% and 60%) under all levels of Reynolds number from 200 to 700.

Therefore, in general we conclude that for negligible to mild arterial stenoses, pressure drop alone is not sufficient to infer the axial symmetricity of the stenosis. But

Figure 5.4: A simplification of Figure 1b in [17]. The shaded region denotes

with severe, more significant arterial stenoses, the pressure drop downstream to the constriction can be an indicator for the stenosis shape and axial symmetricity.

5.2 Comparison with experimental results

While a quantitative comparison with experimental results by [17] is troublesome due to the very different set-up of experiments and the fact that they present limited data on pressure in the paper, we will discuss qualitatively. We observe generally similar pressure distributions for axisymmetric and nonsymmetric geometries. In particular, recall the two-phase pressure increase downstream the throat of stenosis as we described on page 26. A same pattern is present in their axisymmetric models. In their nonsymmetric models, after the phase of "sharp bounce" (see Figure 5.2b), the pressure decreases until it exits from the stenotic segment. This is a result of fluid separation and turbulence in the corner downstream of the stenosis, as shown by the shaded portion in Figure 5.4. In fact, the "stable" phase of pressure distribution in our result can be considered as a counterpart of such pressure decrease. The smoothed stenosis geometry in this thesis reduces the region of this corner and, as a result, induces less turbulent flow.

5.3 Future works and applications

While this thesis has demonstrated the potential of using pressure distribution as an indicator for stenosis geometry and axial symmetricity, in terms of clinical applications,

more works could be done. Also, some extending scopes arise naturally from and are inspired by this study. We introduce some of them in this section.

Comparison database Comparing the numerical results obtained from idealized geometries, we have shown that the pressure drop can differentiate between axisymmetric and nonsymmetric stenoses with significant narrowing in lumen area. However, the numerical values of pressure drop are in general not readily applicable in practical comparisons with patient-specific data. Therefore, a database could be built based on larger number of numerical experiments, followed up by clinical comparisons, so that given a patient-specific measure of blood pressure drop, we can infer the shape of stenosis with good confidence.

Critical cutting length We also notice that downstream of the stenosis, the pressure recovery takes place over different lengths in different models regarding to Reynolds number, severity of stenosis and symmetricity. Important information is possibly lost if downstream geometries are cut before the pressure fully recovers. Therefore, how these factors have impacts on the pressure recovery lengths can be another important issue to study.

Bibliography

[1] J. Ahrens, B. Geveci, C. Law, C. Hansen, and C. Johnson, *36-paraview: An end-user tool for large-data visualization*, The Visualization Handbook, (2005), p. 717.

[2] H. I. Andersson, R. Halden, and T. Glomsaker, *Effects of surface irregularities on flow resistance in differently shaped arterial stenoses*, Journal of Biomechanics, 33 (2000), pp. 1257–1262.

[3] G. K. Batchelor, *An introduction to fluid dynamics*, Cambridge university press, 2000.

[4] S. Chakravarty and P. Mandal, *Mathematical modelling of blood flow through an overlapping arterial stenosis*, Mathematical and computer modelling, 19 (1994), pp. 59–70.

[5] P. Cignoni, M. Callieri, M. Corsini, M. Dellepiane, F. Ganovelli, and G. Ranzuglia, *MeshLab: an Open-Source Mesh Processing Tool*, in Eurographics Italian Chapter Conference, V. Scarano, R. D. Chiara, and U. Erra, eds., The Eurographics Association, 2008.

[6] F. Hecht, *New development in freefem++*, J. Numer. Math., 20 (2012), pp. 251–265.

[7] P. R. Johnston and D. Kilpatrick, *Mathematical modelling of flow through an irregular arterial stenosis*, Journal of Biomechanics, 24 (1991), pp. 1069–1077.

[8] O. A. Karakashian, *On a galerkin–lagrange multiplier method for the stationary navier–stokes equations*, SIAM Journal on Numerical Analysis, 19 (1982), pp. 909–923.

[9] S. E. Logan, *On the fluid mechanics of human coronary artery stenosis*, IEEE Transactions on biomedical engineering, (1975), pp. 327–334.

[10] W. Nichols and M. ORourke, *McDonalds Blood Flow in Arteries: Theoretic, Experimental and Clinical Principles*, Lea & Febiger, 1990.

[11] A. Quarteroni, *Numerical models for differential problems*, vol. 2, Springer Science & Business Media, 2010.

[12] A. Quarteroni, A. Veneziani, and C. Vergara, *Geometric multiscale modeling of the cardiovascular system, between theory and practice*, Computer Methods in Applied Mechanics and Engineering, 302 (2016), pp. 193–252.

[13] R. M. Tayebi, R. Wirza, P. S. Sulaiman, M. Z. Dimon, F. Khalid, A. Al-Surmi, and S. Mazaheri, *3d multimodal cardiac data reconstruction using angiography and computerized tomographic angiography registration*, Journal of cardiothoracic surgery, 10 (2015), p. 58.

[14] A. Viguerie and A. Veneziani, *Inexact algebraic factorization methods for the steady incompressible navier stokes equations at moderate reynolds numbers*, (Submitted).

[15] A. Y. Wong, G. Klassen, and D. E. Johnstone, *Hemodynamics of coronary artery stenosis*, Canadian journal of physiology and pharmacology, 62 (1984), pp. 59–69.

[16] D. Young, *Effect of a time-dependent stenosis on flow through a tube*, ASME, 1967.

[17] D. F. Young and F. Y. Tsai, *Flow characteristics in models of arterial stenoses - i. steady flow*, Journal of biomechanics, 6 (1973).